

# Deep basin conductor characterization using machine learning-assisted magnetotelluric Bayesian inversion in the SW Barents Sea

Romain Corseri<sup>1,2,\*</sup>, Hoël Seillé<sup>3</sup>, Jan Inge Faleide<sup>1</sup>, Sverre Planke<sup>1,2</sup>, Kim Senger<sup>4</sup>, Mohamed Mansour Abdelmalak<sup>1,2</sup>, Leiv Jacob Gelius<sup>1</sup>, Geoffroy Mohn<sup>5</sup>, and Gerhard Visser<sup>3</sup>

<sup>1</sup>University of Oslo, Department of Geosciences, 0371 Oslo, Norway

<sup>2</sup>Volcanic Basin Energy Research AS, 0361 Oslo, Norway

<sup>3</sup>CSIRO, Deep Earth Imaging FSP, Australian Research Centre, Kensington,  
WA6151, Australia

<sup>4</sup>The University Centre in Svalbard (UNIS), Department of Arctic Geology,  
9171 Longyearbyen, Norway

<sup>5</sup>Université de Cergy Pontoise, Département Géosciences et Environnement  
(GEC), Neuville-sur-Oise, 95000, France

\*corresponding author: roman.corseri@geo.uio.no

June 26, 2023

## Summary

In this article, we use a new workflow to substantiate the characterization of a prominent, deep sediment conductor in the hyper-extended Bjørnøya Basin (SW Barents Sea) previously identified in smooth resistivity models from 3D deterministic inversion of magnetotelluric data. In low dimensionality environments like layered sedimentary basin, 1D Bayesian inversion can be advantageous for a thorough exploration of the solution space but the violation of the 1D assumption has to be efficiently handled. The primary geological objectives of this work is therefore preceded by a secondary task: the implementation of a new machine learning approach for handling the 1D violation assumption for 21 MT field stations in the Barents Sea. We find that a decision tree can adequately learn the relationship between MT dimensionality parameters and the 1D-3D residual response for a training set of synthetic models, mimicking typical resistivity structures of the SW Barents Sea. The machine learning model is then used to predict the dimensionality compensation error for MT signal periods ranging of 1 to 3000 s for 21 receivers located over the Bjørnøya Basin and Veslemøy High. After running 1D Bayesian inversion, we generated a posterior resistivity distribution for an ensemble of 6000 1D models fitting the compensated MT data for each 21 field stations. The proportion of 1D models showing  $\rho < 1 \Omega.m$  is consistently beyond 80% and systemically reaches a maximum of 100% in the Early Aptian - Albian interval in the Bjørnøya Basin. In hyper-extended basins of the SW Barents Sea, the dimensionality compensation workflow has permitted to refine the characterization of the deep basin conductor by leveraging the increased vertical resolution and optimal used of MT data. In comparison, the smooth 3D deterministic models only poorly constrained depth and lateral extent of the basin anomaly. The highest probability of finding  $\rho < 1 \Omega.m$  is robustly assigned to the syn-tectonic Early Aptian - Albian marine shales, now buried at 6 to 8 km depth. Based on a theoretical two phase fluid-rock model, we show that the pore fluid of these marine shales must have a higher salinity than seawater to explain the anomaly  $\rho < 1 \Omega.m$ . Therefore, the primary pore fluid underwent mixing with a secondary brine during rifting. Using analogue rift systems in paleomargins, we argue that two possible secondary brine reservoir may contribute to deep saline fluid circulation in the hyper-extended basin: (1) Permian salt-derived fluid and, (2) mantle-reacted fluid from serpentinization.

# 1 Introduction

3D deterministic inversion of magnetotelluric (MT) data is an appealing approach because it provides an accurate representation of the subsurface resistivity structure. However, it often relies on a coarse model discretisation because of the high computational cost and produces a single preferred model, obtained by balancing roughness and data fit.

In the Barents Sea (Figure 1), geometrical properties of the MT phase tensor (Caldwell et al., 2004) reveals significant 2D and 3D effects in the MT data and complex directionality of the underlying conductivity structures (Corseri et al., 2021). 1D or 2D inversion of data affected by 3D effects are likely to introduce artefacts in the resistivity models (Jones, 2012; Ledo, 2005) so in a previous study (Corseri et al., 2023), we favored a 3D approach using ModEM (Kelbert et al., 2014). A prominent anomalous conductor ( $\rho < 1 \Omega.m$ ) is identified within the deep sedimentary strata of the Bjørnøya Basin and in the westernmost part of the Veslemøy High between 6 and 12 km at depth (Figure 2). However, due to the heavy regularization applied to the model, it is challenging to fully characterize this sediment-related anomaly, assign it a depth interval and interpret the geological processes behind the high electrical conductivity (Corseri et al., 2023).

In MT stations located over the Bjørnøya Basin, analysis of the MT phase tensor (Corseri et al., 2021) reveals low dimensionality effects down to periods of 100-200 seconds. Therefore, a 1D probabilistic inversion approach could be advantageous and provide new constraints on the conductivity anomaly by benefiting from increased vertical resolution, thorough exploration of the solution space and optimal utilisation of high quality MT data. Nevertheless, the approach requires handling of the 1D modelling assumption violation in the MT data.

In this work, we utilize a workflow developed by Seillé and Visser (2020) which quantitatively handles the violation of the 1D assumption for a more appropriate application of 1D Bayesian inversion. Instead of using large errors floors or removing data points presenting 2D or 3D effects to compensate for the modelling assumption, Seillé and Visser (2020) uses a Machine Learning (ML) algorithm trained on a synthetic MT database to learn a relationship between 1D and 3D MT responses (Figure 3a).

The overarching goals of this study are thereby two-folds: (1) a methodological objective that

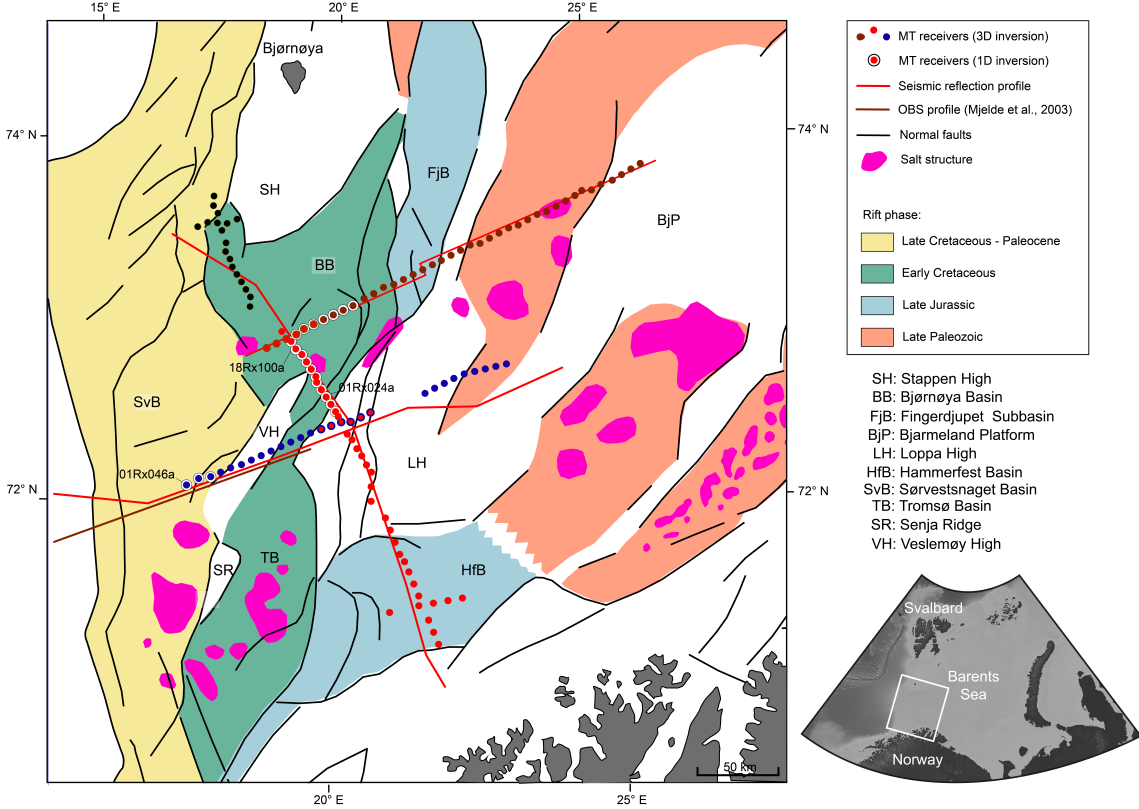


Figure 1: Location map of the selected MT receivers in the SW Barents Sea, overlain on structural elements and principal rift phases (Faleide et al., 2008). The inset map (in polar projection, bottom right) shows the study area in a wider Barents Sea context.

aims at using a newly developed dimensionality compensation workflow with ML and, (2) a geological objective that aims at refining the characterization of a prominent deep basin conductor in the SW Barents Sea. To achieve these goals, we first adapt the dimensionality compensation workflow (Seillé and Visser, 2020) to the Barents Sea geological context and to the depth of investigation of our geological target, a deep basin conductor. 3D resistivity models are built to generate a synthetic MT database that contains sufficient dimensionality effects and can mimic adequately the geology of the Barents Sea. Secondly, after training the ML algorithm and applying the error model, we perform 1D Bayesian inversion over a selection of 21 receivers located over the Bjørnøya Basin and the Veslemøy High, an inverted Cretaceous high in the SW Barents Sea (Figure 1; Lundin and Doré, 2019). Then, we characterize the prominent basin conductor ( $\rho < 1 \Omega.m$ ) with a statistical analysis of the posterior model distribution and compare the probabilities with the anomaly in 3D deterministic models. Finally, we use the Hashin-Shtrikman upper conductivity bound model (Hashin and Shtrikman, 1962) constrained by fluid salinity and mineralogy of rock samples from detachments faults in paleomargins (Corre

et al., 2018; Nteme Mukonzo et al., 2021; Pinto et al., 2015; Quesnel et al., 2019; Salardon et al., 2017) to unveil two conceptual models of brine circulation in hyper-extended rift systems.

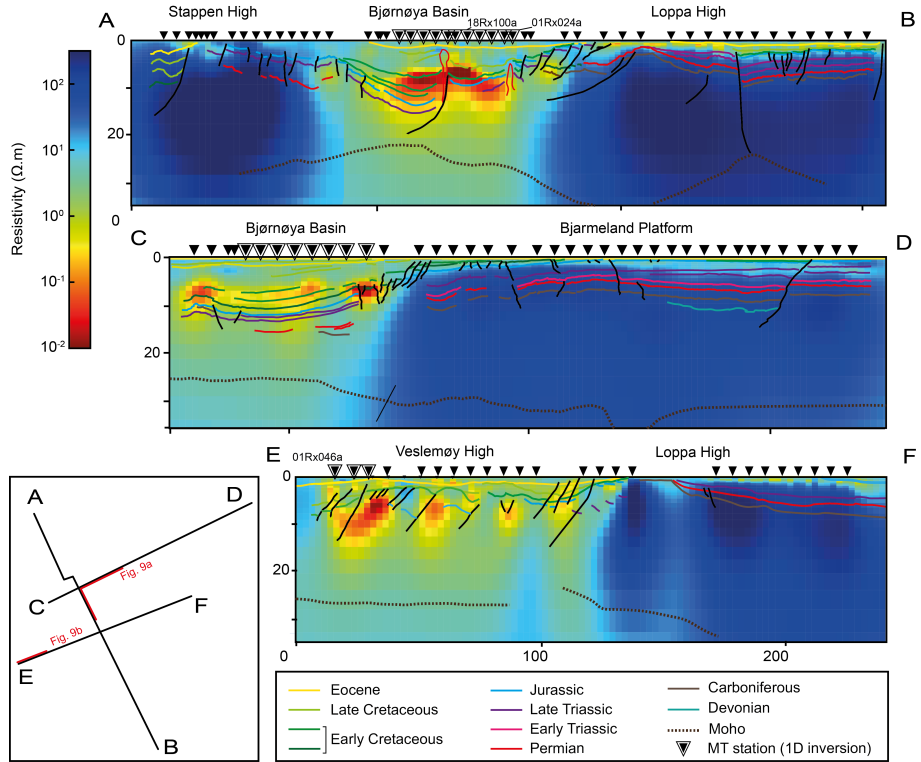


Figure 2: Summary of the 3D deterministic inversion results in the SW Barents Sea from Corseri et al. (2023). The E-F MT profile (or EW3 profile), over the Veslemøy High, is a new addition to the 3D deterministic models with an overall normalized RMS value of 0.93 over the four components of the impedance tensor. See Figure 1 for depth section and receiver location over the structural elements of the SW Barents Sea

## 2 Data and Method

### 2.1 MT data

The 123 receivers selected for 3D deterministic inversion (Figure 2) are shown in Figure 1. They represent a subset of a 337 receiver database in the SW Barents Sea where MT data were extracted as a byproduct of controlled-source electromagnetic (CSEM) surveys (Corseri et al., 2021). A good quality MT signal is obtained for a period range of 1 to 3000 s, on average. Focusing on the refining the deep basin conductor, we apply the dimensionality compensation workflow and perform the 1D Bayesian inversion to 21 receivers located over the hyper-extended Bjørnøya Basin and Veslemøy High (Figure 1).

## 2.2 Workflows

The methodology is separated into two parts, with outputs from the first one serving as input to the second (Figure 3). They were originally developed by Seillé and Visser (2020) in sedimentary basins onshore Australia for mineral exploration.

The first task is to train a supervised Machine Learning (ML) model to recognize dimensionality effects in magnetotelluric data. The ML algorithm takes as input a synthetic database generated from 3D resistivity models (Figure 3a). A relationship is learnt between geometrical properties of the MT phase tensor  $\Phi$  and the difference between the 3D resistivity model response and the 1D resistivity column response located directly beneath the receiver. This calculation is repeated for each MT station of the 3D models in the training ensemble. The MT phase tensor  $\Phi$  is related to the MT impedance tensor  $\mathbf{Z}$  as:

$$\Phi = X^{-1}Y \text{ where } Z = X + iY \quad (1)$$

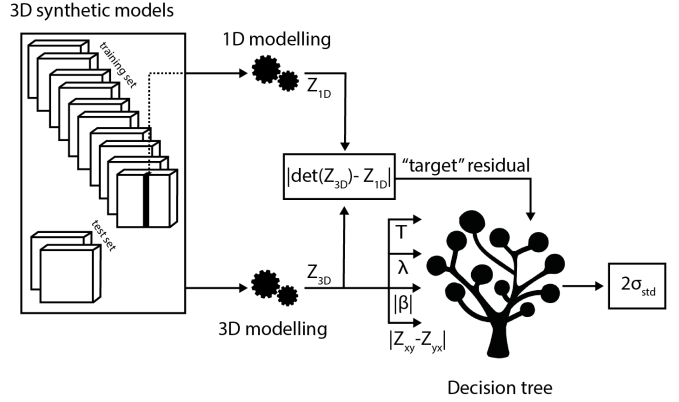
$\mathbf{X}$  and  $\mathbf{Y}$  are the real and imaginary part of the complex tensor  $\mathbf{Z}$ .

In the second part, the geometrical properties of the field MT data are passed into the ML model trained in the first part of the workflow (Figure 3b). The output of the ML model is the prediction of the standard deviation to apply to each MT stations at each frequencies given the modelling assumption of the forward operator. In the Bayesian 1D inversion framework, the modeled MT data can be formulated as:

$$d = g(m) + \eta + \nu \quad (2)$$

where  $\nu$  represents the error due the 1D-physics assumption and  $\eta$ , the processing error.  $g()$  is the magnetotelluric forward operator and  $m$  is the resistivity column extracted beneath the receiver in the 3D resistivity model. The goal of the first part of the workflow is to learn  $\nu$  (Figure 3a). In the second part, we derive  $\nu$  with the trained ML model and apply the "modelling assumption" error to the field data. The compensated MT data are then used in to the 1D Bayesian inversion (BMT1Dinv, Seillé and Visser, 2021) to explore the solution space and find an ensemble of 1D resistivity model that fits the observations within the uncertainty of the 1D-physics assumption (Figure 3b). The two following sections provide more details on the two tasks described in this paragraph.

### a. Learning dimensionality compensation



### b. Bayesian inversion considering dimensionality discrepancies

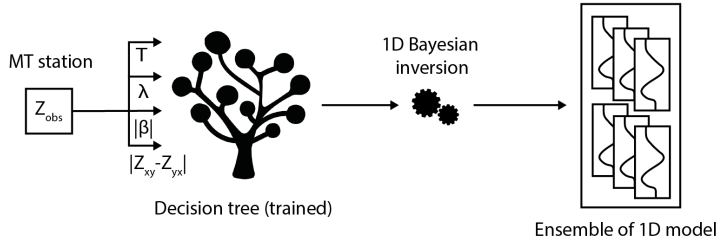


Figure 3: Simplified illustrations of the two workflows used in this study, originally developed by Seillé and Visser (2020). Workflow a) depicts the training of the decision tree from synthetic MT data to learn dimensionality compensation. In workflow b), we use the trained ML model in part a) to assign a "1D Earth" modelling error to the field data before feeding them to the 1D Bayesian inversion process.  $Z_{obs}$  is the observed MT impedance tensor in the SW Barents Sea.  $Z_{3D}$  is the MT impedance tensor response of the 3D synthetic model while  $Z_{1D}$  is the response of the synthetic resistivity column.  $T$  is the signal period.  $\lambda$  and  $\beta$  are, respectively, ellipticity and skew angle of the 3D response (Equations (3) and (4)).  $Z_{xy}$  and  $Z_{yx}$  are the two non-diagonal elements of  $Z$  expressed in Cartesian coordinates.

## 2.3 Learning dimensionality discrepancies with a decision tree

### 2.3.1 3D synthetic resistivity model ensemble

We populate a total of twelve 3D resistivity models divided into a training (ten models) and validation set (two models) (Figure 4). The resistivity features of the models are randomly-generated and adapted to the Barents Sea context. The models are made of eight sedimentary layers, a resistive crystalline crust and two geobodies. Each sedimentary layer resistivity follows a normal distribution centered around a value comprised between 1 and 100  $\Omega \cdot m$  and a standard deviation of 25% of the average value. The chosen average resistivity values for

the sedimentary layers reflect the values observed in well logs in the SW Barents Sea. The crystalline crust resistivity follows a normal distribution centered around  $3100 \Omega\text{-m}$ . Horizontal resistivity variation are also allowed within the crust. The layers are vertically deformed so that the depth to the crust could vary between 0 and 20 km, thereby reflecting the variety of sedimentary basin depth in the Barents Sea. Two major faults are inserted in the resistivity models with random vertical throws and orientations. Finally, two randomly generated potato-shaped bodies are inserted. One has a high resistivity centered around  $10000 \Omega\text{-m}$ , reflecting the possible presence of salt diapirs or igneous intrusions. The second has very low resistivity ( $0.1 \Omega\text{-m}$ ), mimicking the presence of a melt reservoir, mineralized body or saline fluids. Two examples of 3D models are depicted in Figure 4.

Horizontally, the model is discretized into 81 cells of 3.5 by 3.5 km in the core area. In the vertical direction, the model is made of 49 cells starting with 50 m thickness at the surface and then increasing with a 1.1 factor, up to 5 km thickness for the last cell of the core area at 52 km depth. The padding area is made of 4 cells with dimensions growing with factor of 1.6 in all directions.

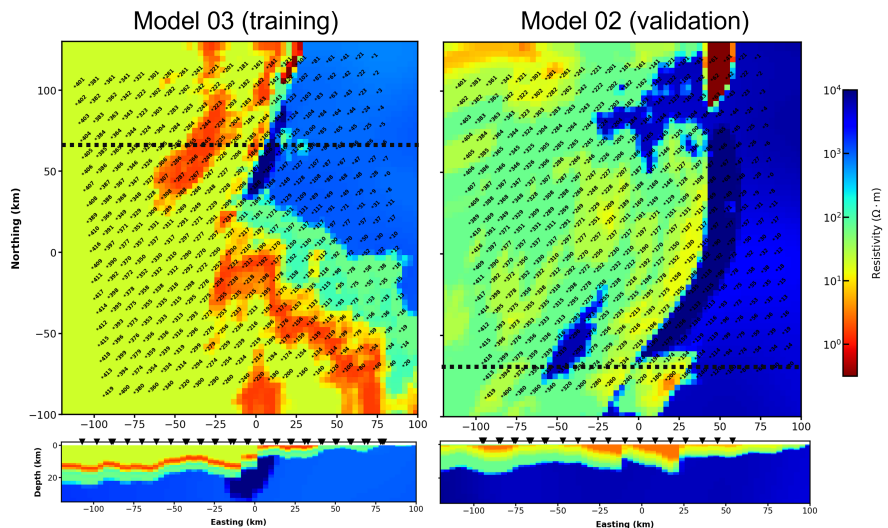


Figure 4: Two randomly generated 3D resistivity models displayed at a depth of 8.2 km (upper panels) and E-W profiles (lower panels). The dashed line indicates the location of the profile on the depth slice. The grid is made of 420 receivers, depicted by black triangles.

### 2.3.2 Generating training MT data and 1D-3D target residuals

The MT data are modelled using the 3D forward engine of ModEM (Kelbert et al., 2014). We generate the data over a regular grid of 420 receivers, laid along 20 E-W lines of 21 receivers. The receiver separation is 10 km (Figure 4). We compute the four components of the MT impedance tensor  $\mathbf{Z}$  for 24 periods ranging from 0.7 to 3000 s. The modelled period content is the same as the field data in the Barents Sea (Corseri et al., 2021; Corseri et al., 2023). Consequently, the training set is made of 100800 data points, generated over 420 receivers, 24 periods for ten 3D resistivity models. The validation set is made of 20160 data points, representing approximately 17% of the whole synthetic set.

As pictured in Figure 3a, the 1D-3D residual response is defined as the modulus of the difference between the determinant of the MT impedance tensor of the 3D model and the response of the 1D resistivity column located directly beneath the station:  $residual = |det(Z_{3D}) - Z_{1D}|$ . This calculation is repeated for each station and each period. The extraction of the 1D resistivity column, subsequent calculation of the 1D forward MT response and residuals are all scripted in Python.

### 2.3.3 Decision tree: inputs, attributes and basic algorithm description

Analysis of invariants of the phase tensor is commonly used to derive dimensionality information and justify a modelling approach (Bibby et al., 2005; Caldwell et al., 2004). The inputs of the machine learning model are (1)  $T$  signal period, (2)  $|Z_{xy} - Z_{yx}|$ , (3) the skew angle  $\beta$  and (4) the ellipticity  $\lambda$ . They can be expressed as function of the four components  $\Phi_{ij}$  of the phase tensor (Equation (1)):

$$\beta = \frac{1}{2} \arctan\left(\frac{\Phi_{12} - \Phi_{21}}{\Phi_{11} - \Phi_{22}}\right) \quad (3)$$

$$\lambda = \sqrt{\frac{(\Phi_{11} - \Phi_{22})^2 + (\Phi_{12} + \Phi_{21})^2}{(\Phi_{11} + \Phi_{22})^2 + (\Phi_{12} - \Phi_{21})^2}} \quad (4)$$

Caldwell et al. (2004) have evaluated threshold values of  $\beta$  and  $\lambda$  that form necessary conditions for dimensionality:

(i) 1D:  $|\beta| < 3^\circ$  and  $\lambda < 0.1$

(ii) 2D:  $|\beta| < 3^\circ$  and  $\lambda > 0.1$

(iii) 3D:  $|\beta| > 3^\circ$  and  $\lambda > 0.1$

A decision tree is a type of machine learning algorithm used for both classification and regression tasks. It typically uses conditions on input variable like (i), (ii) and (iii) as attributes. The algorithm works by partitioning the target feature (here, the residuals) based on the inputs values, using a tree-like structure. Each node in the tree represents a descriptive feature or attributes on which the tree can split into two branches based on decision on the given attribute. The leaves of the tree represent the final output, which in our case corresponds to the standard deviation (dimensionality discrepancy "noise") to apply to the data. The tree is grown recursively starting from the root node, by selecting the best feature to split the dataset based on information gain. Our decision tree is trained using an algorithm written in the Julia programming language (Julia Language, <https://julialang.org/>) using the attributes (Table 1) selected onshore Australia (Seillé and Visser, 2020).

$ \beta $	$\lambda$	$ Z_{xy} - Z_{yx} $
$ \beta  < 2$	$\lambda < 0.1$	$\log( Z_{xy} - Z_{yx} ) < 0.1$
$2 <  \beta  < 3$	$0.1 < \lambda < 0.2$	$0.1 < \log( Z_{xy} - Z_{yx} ) < 0.3$
$3 <  \beta  < 5$	$0.2 < \lambda < 0.3$	$0.3 < \log( Z_{xy} - Z_{yx} ) < 0.5$
$5 <  \beta  < 7$	$0.3 < \lambda < 0.4$	$0.5 < \log( Z_{xy} - Z_{yx} )$
$7 <  \beta  < 9$	$0.4 < \lambda < 0.5$	-
$9 <  \beta $	$0.5 < \lambda < 0.75$	-
-	$0.75 < \lambda$	-

Table 1: Attribute features of the decision tree from Seillé and Visser (2020)

## 2.4 1D Bayesian inversion

In a Bayesian inversion framework, solving the inverse problem consists in determining a posterior probability distribution  $p(m | d)$  on the model parameters  $m$  given the observed data  $d$  (Tarantola, 2005). This posterior resistivity distribution is approximated by an ensemble of models that are consistent with the observed data within its uncertainty. This is the fundamental difference with deterministic inversion where the solution consists in a single best-fit model. The posterior probability distribution  $p(m | d)$  is obtained following Bayes' theorem:

$$p(m | d) = \frac{p(d | m)p(m)}{p(d)} \quad (5)$$

The prior distribution  $p(m)$  defines our prior knowledge about the distribution of the model parameters. The likelihood function  $p(d | m)$  defines the goodness-of-fit of the model to the

observed data. In this study we sample  $p(m | d)$  using a trans-dimensional Markov chain Monte Carlo (McMC) algorithm (Seillé and Visser, 2020), where the models can have varying number of dimensions, i.e 1D models with varying number of layers. We use a likelihood function given by:

$$p(d | m) \propto \exp\left(-\frac{1}{2}(d_{obs} - g(m))^T C_d^{-1}(d_{obs} - g(m))\right) \quad (6)$$

where  $d_{obs}$  denotes the observed data,  $g(m)$  is the magnetotelluric forward operator for model  $m$  and  $C_d^{-1}$  is the inverse of the data covariance matrix. Here, we consider the error due to the 1D-physics assumption ( $\nu$  in Equation (2)) derived from the regression tree, and the processing error ( $\eta$  in Equation (2)).  $C_d$  is a diagonal matrix defined as:  $C_d = \text{diag}(\nu^2) + \text{diag}(\eta^2)$ . More details on the McMC algorithm used in our study are given in Seillé and Visser (2020).

## 3 Machine learning model evaluation and application to field data

### 3.1 Suitability of training data

To achieve an adequate training of the decision tree, it is crucial that the 3D models generate enough 2D and 3D effects in the response so the training data (the dimensionality invariants  $\lambda$  and  $\beta$  in Figure 3) can be representative of the geometrical properties of field MT data. Otherwise, the ML model would not generalize to real data and produce inadequate dimensionality errors, biasing the 1D resistivity ensembles from the probabilistic inversion. Figure 5 shows the normalized distribution of the input parameters  $\lambda$  and  $\beta$  data used in the training and observed data sets. We observe that the training data are representative of observations in the Barents Sea, containing a sufficient amount of 2D and 3D effects.

### 3.2 Model performance

To test our trained model, we used the validation dataset computed over two synthetic 3D models. The decision tree performance on learning a relationship between dimensionality invariants and 1D-3D residuals is assessed using the mean squared error (MSE) as metrics (See Equation (1) in Supplementary Materials). We calculate the average MSE for four consecutive periods ranges [0.1-1], [1-10], [10-100] and [100-3000] in Figure 6.

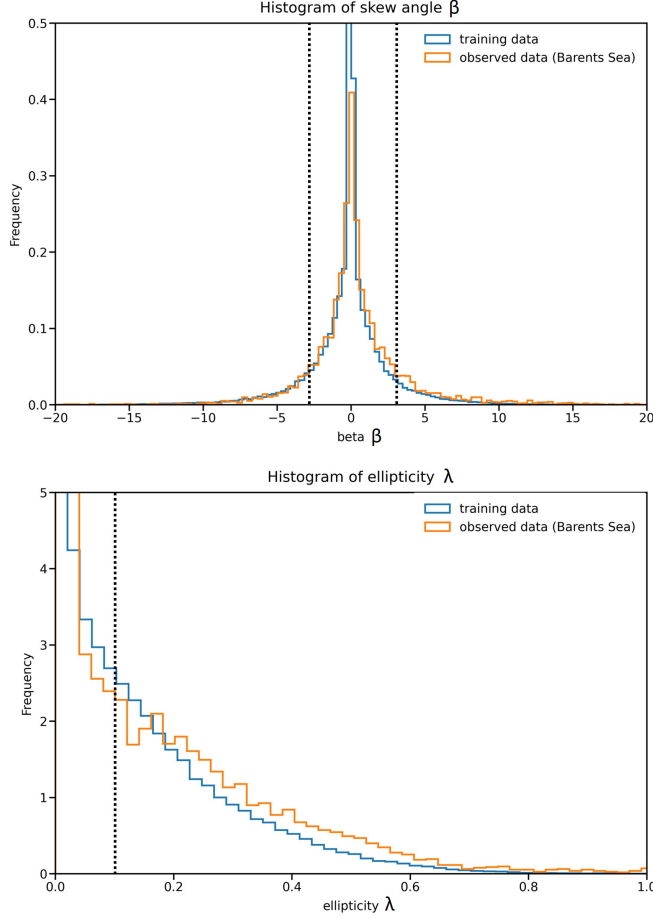


Figure 5: Normalized distributions of skew angle  $\beta$  (upper plot) and ellipticity  $\lambda$  (lower plot) values for training and observed dataset in the SW Barents Sea. The training set is made  $n=100800$  data points while the test set contains  $n= 20160$  data points.

First, we observe that the training MSE is low and within 0.02 to 0.1 for the four period ranges with a slight upward trend consistent with increasing 3D effects (or data complexity) at longer periods. The training MSE reaches a maximum of 0.1 for [100-3000 s] and stands out as five times higher than the shortest period range. The noisiness and increased complexity of the data at these long periods are the two main reasons for the slightly lower ML model performance at  $T > 100$  s. Surprisingly, the test or validation error are systematically lower than the training error, probably due to a random effect on the choice of the test data. It confirms the ML model is not overfitting the training data.

As a result, we consider that the trained decision tree adequately represents the dimensionality effects in the field data.

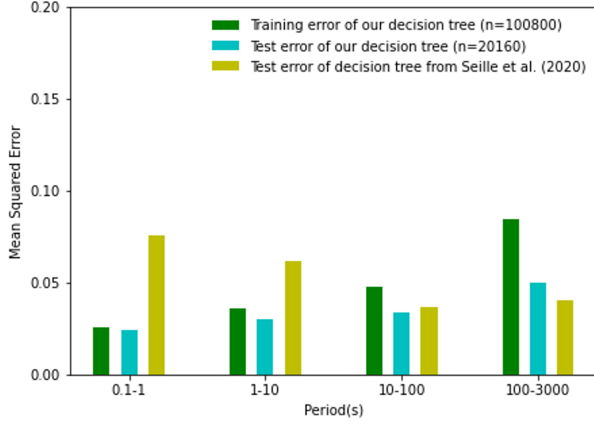


Figure 6: Training and test Mean Squared Error of the decision tree for four period ranges. For comparative purposes, we also show the prediction error of the decision tree from Seillé and Visser (2020) taking the test data generated in this study as input.

### 3.3 Applying dimensionality compensation to MT data in the SW Barents Sea

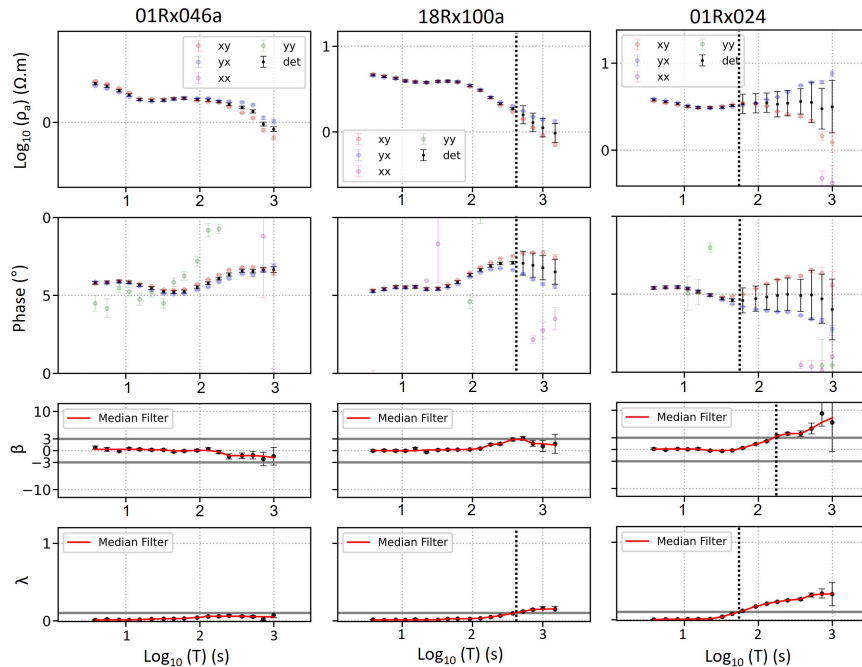


Figure 7: MT data and associated determinant values after prediction of the dimensionality error model, for three receivers in the SW Barents Sea. In the two lower panels, The dimensionality indicators  $\lambda$  and  $\beta$  values are plotted as function of periods. The vertical dashed lines mark the violation of the 1D modelling assumption and correspond visually to the increasing standard deviation in the MT data.

We apply the second part of the workflow (Figure 3b) and pass a selection of 21 MT stations (Figure 1) into the grown decision tree. A graphical rendition of the grown decision tree is given in Fig. S1 in the Supplementary Materials.

The output is the predicted standard deviation to apply to each data point to compensate for the inadequate 1D modelling assumption. We illustrate the prediction for three receivers where the 2D and 3D effects influence the MT data at very different periods ranges (Figure 7). For receiver 01Rx046a, we observe that the combination of  $\lambda$  and  $\beta$  entails a 1D dimensionality at all periods. Consequently, the applied standard deviation is very low at all periods, corresponding to the processing noise. At receiver 18Rx100a, ellipticity  $\lambda$  values are superior to 0.1 for  $T > 500$  s and thereby violate the 1D assumption. This is reflected in the relaxed standard deviation predicted by the decision tree for  $T > 500$  s. At 01Rx024a, the necessary conditions for 1D modelling are violated at  $T > 80$  s for  $\lambda$  and  $T > 100$  s for  $\beta$  with both inputs increasing with periods.

In conclusion, the predicted dimensionality compensation is therefore visibly increasing with periods and reaches a maximum value at  $T = 1000$  s. The predicted results for field data into the trained ML model is visibly adequate in the Barents Sea. The dimensionality compensation can be safely applied to the selection of receivers, which in turn will be used in the 1D Bayesian inversion process.

## 4 1D MT Bayesian inversion in the SW Barents Sea

### 4.1 1D posterior resistivity distributions

The 1D Bayesian inversion is run for a selection of 21 receivers (Figure 1) located over an anomalous conductor identified in 3D deterministic inversion models in the Bjørnøya Basin (Corseri et al., 2023) and the westernmost part of the Veslemøy High (Figure 2). Here, we take advantage of the low dimensionality in the MT data up to periods  $T = 100 - 200$  s (Figure 7). Because the 1D trans-dimensional inversion approach has no vertical discretization limitation, it can improve the characterisation of the basin conductor with higher accuracy than the heavily regularized 3D inversion. This probabilistic inversion study will focus on the basin sediments down to the Late Jurassic horizon or to 14 km depth where no seismic interpretation allows to define the base of sediments.

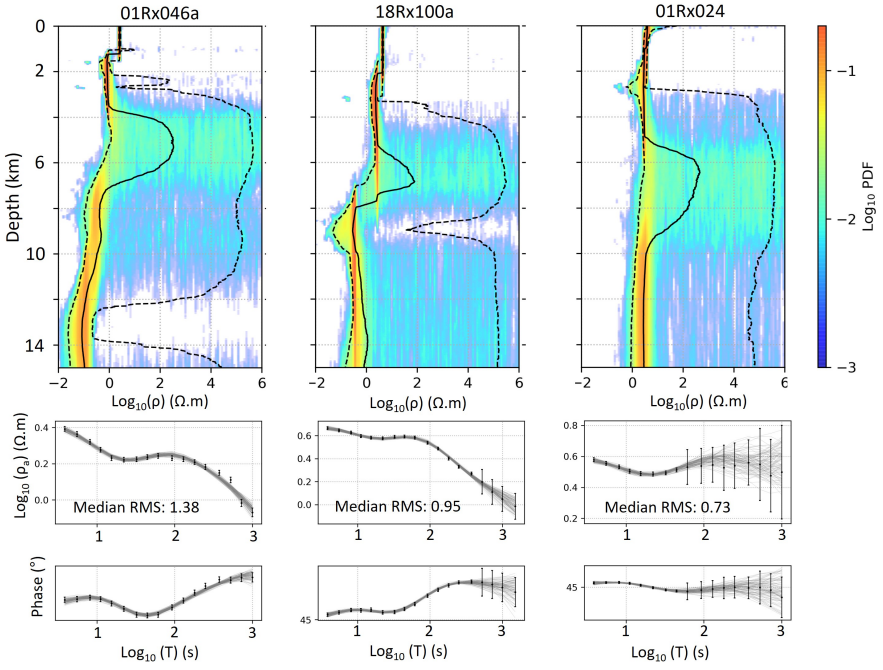


Figure 8: Posterior probability density distributions or Probability Density Function (PDF) (upper panel) and MT responses (Lower panel) for three receivers marked in Figure 1. 01Rx046a (left) is located in the Veslemøy High, 18Rx100a and 01Rx024 in the Bjørnøya Basin. In the posterior density distribution, the solid black line represent the median model, the dashed black lines stand for the 5<sup>th</sup> and 95<sup>th</sup> percentiles to capture the uncertainty associated with the median value.

The prior probability distribution of the resistivity is uniform between  $10^{-2}$  and  $10^6 \Omega.m$ . The prior distribution on the number of layers is also adapted so the inversion will favor model complexity in the first 20 km and minimize it in the deepest part of model where sensitivity is limited or absent. The inversion is run for each receiver using 60 chains of  $10^6$  simulations each, allowing convergence. For all receivers, the 1D model ensemble has a low median RMS value between 0.7 and 1.95. The posterior probability distribution for each receiver is defined by an ensemble of 6000 1D models.

The posterior probability distributions for three receives are shown in Figure 8 along with the MT responses. The 1D posterior distributions for all 21 receivers are provided in Supplementary Materials (Figures S2 and S3). In the first 3 km, we observe that there is little spread in the resistivity distribution across the ensembles, 1-10  $\Omega.m$  for all three receivers constrained in

1 to 3 layers.

For 01Rx046a, the spread of resistivity values becomes extremely broad  $1 - 10^5 \Omega.m$  between 4 and 6 km before most models requiring resistivity values beneath  $0.5 \Omega.m$  at 6 km and deeper, thereby defining a possible interface for the top of the conductor.

For 18Rx100a, we observe a bimodal density distribution between 7 to 8 km where most resistivity values are divided into either  $\sim 0.5$  or  $8 \Omega.m$ . Between 8 to 10 km, the high proportion of models points to low resistivity values  $\rho < 1 \Omega.m$  thereby defining a high probability of finding highly conductive sediments within this interval. Beneath 10 km, the resistivity variability is higher (but still indicative of low resistivity), likely reflecting the relaxing of the data error at long periods due to 3D effects.

For 01Rx024a, we see no indications of low resistivity values  $\rho < 1 \Omega.m$  in the ensemble and the broad range of resistivity for depth  $> 3 \text{ km}$  reflects the domination of 2D and 3D effects in the MT data at shorter periods ( $\sim 700$  seconds) and the increased predicted standard deviation by the dimensionality error model (Figure 7).

## 4.2 Conditional resistivity distributions

We calculate the conditional probability distribution of resistivity models to reach value lower than  $1 \Omega.m$ . Assuming that every model in the ensemble has the same probability to occur, we count the number of models having  $\rho < 1 \Omega.m$  at a 150 meters interval and divide by the total number of models in the ensemble.

In Figure 9, we represent the conditional model distribution overlain on interpreted depth sections and 3D resistivity models of the Bjørnøya Basin and Veslemøy High (Figures 1 and 2). Focusing on finding 1D models fulfilling the condition  $\rho < 1 \Omega.m$  in the deep basin sediments (from 4 km depth down to Late Jurassic level), we find that a maximal probability (close to 1) is systematically obtained in the stratigraphic intervals defined by the base Aptian and intra Albian seismic horizons in the Bjørnøya Basin (Figure 9a). Where this sediment layer is too thin or does not exist, then we find a very low probability of encountering the condition  $\rho < 1 \Omega.m$ . In the southern part of the Bjørnøya Basin, we observe  $\rho < 1 \Omega.m$  in 3D models (See 01Rx024a in Figure 9 as an example) whereas the 1D Bayesian inversion results do not.

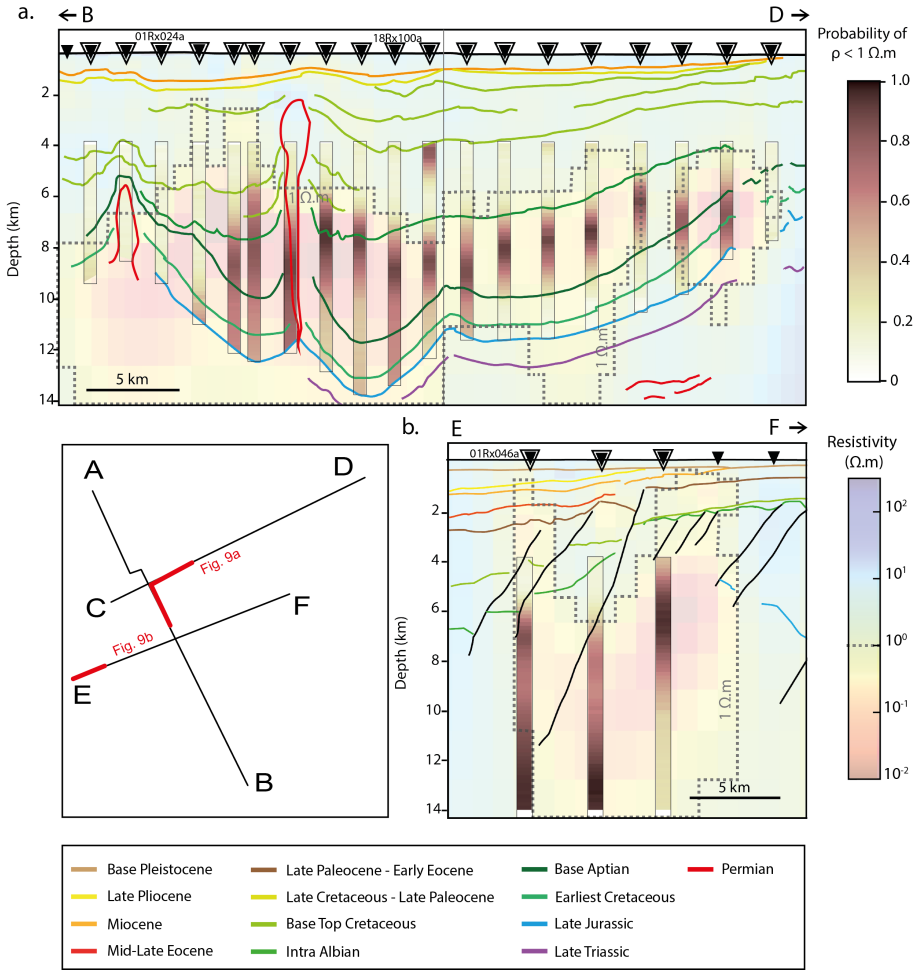


Figure 9: Probability of occurrence of  $\rho < 1 \Omega.m$  from 4 km down to the Late Jurassic horizon (where available), marking the onset of subsidence in a) the Bjørnøya Basin and b) Veslemøy High. See Figure 1 for depth section and receiver location over structural elements of the SW Barents Sea. The probabilities are overlain on the resistivity model from 3D inversion (Figure 2), where the thin dashed line represents the  $1 \Omega.m$  contour.

In Veslemøy High (Figure 9b), the challenging seismic imaging below the Top Cretaceous horizon makes the assignment of a stratigraphic interval difficult. Interestingly, we observe two probability maxima at 01Rx046: a first around 7 km and a second one beneath 13 km. The shallowest maxima is obtained at the easternmost receiver at 6 - 7 km. We observe  $\rho < 1 \Omega.m$  in younger Cenozoic sediments in 3D inversion models whereas with 1D Bayesian process, the conductor is systematically located below the Top Cretaceous horizon.

## 5 Discussion

### 5.1 Performance of the workflows in the SW Barents Sea

We argue that this study shows that the workflow created by Seillé and Visser (2020) is applicable to a different geological context and MT period content. To train our new ML model, we have adapted the 3D resistivity models to a Barents Sea context with deeper, hyper-extended basins (down to 15 km) and a more conductive sediment overburden. For comparative purposes, we passed our test data (Figure 3) into the Australian-trained ML-model (Seillé and Visser, 2020; Seillé et al., 2021) and calculated the test MSE (Figure 6). We found higher test MSE with the Australian-trained ML-model than the Barents-trained ML-model for the period range 0.1 to 100 s. For a properly trained ML model, this result is expected because the Australian ML-model is trained for a different geological context and depth of investigation with period range from  $10^{-4} - 10$  s versus 0.1 – 3000 s in the Barents Sea. This result confirms that the dimensionality compensation workflows (Seillé and Visser, 2020) works and is adaptable to a different geological target.

In Figure 9, we observe significant discrepancies between the conductive anomaly contour from 3D models and its probability of presence based on 1D Bayesian inversion. Firstly, the top of the  $1 \Omega.m$  contour on 3D models is generally placed shallower and corresponds to close to null probability in 1D model ensemble from Bayesian inversion. This is particularly evident where the 3D anomaly reaches close to the seabed which is not geologically realistic. On the contrary, the probability distribution yields a more consistent vertical placements from receiver to receiver between the Early Aptian and Albian horizons. This fit is slightly degraded for receivers in the vicinity of the largest salt diapir in the Bjørnøya Basin, probably due to large 3D distortion in the data.

Secondly, the lateral continuity of the anomaly is clearly improved with 1D Bayesian inversion where the probability of presence of the conductor vanishes where the Early Aptian - Albian layer pinches out on the side of the basin. On 3D models, the anomaly is laterally discontinued and does not fit with any seismically-defined layers. These results demonstrate the improvements of the anomaly characterisation with the workflow presented in this study.

In Fig. S4 of Supplementary Materials, we show 1D Bayesian inversion results for three differ-

ent ways of handling the 1D-Physics assumption violation: (1) Dimensionality compensation workflow (this study), (2) masking data points containing 2D and 3D effects and (3) error floor. The comparison emphasizes the necessity of handling the 1D modelling error with this workflow in order to avoid losing information on the geological target or overfitting data.

## 5.2 The Aptian-Albian marine shales in the SW Barents Sea

Both 3D deterministic models and statistical analysis of the 1D posterior model distribution consistently identify a highly conductive anomaly in the Early Cretaceous sediments of the hyper-extended basins in the SW Barents Sea (Figures 2 and 8). Using Bayesian inversion, we refine the stratigraphic interpretation by assigning the Early Aptian - Albian age to the basin conductor.

### 5.2.1 Depositional environment and tectonic context

The Early Aptian corresponds to the culmination of Cretaceous rifting in the SW Barents Sea Basins (Serck et al., 2017). In the nascent Early Aptian - Albian Bjørnøya and Tromsø basins (Figure 1), km-thick, fine-grained, hemipelagic muds were deposited in a deep water environment (Corseri et al., 2018; Midtkandal et al., 2019). These marine shales form the lower part of the Aptian - Early Cenomanian Kolmule Formation. Within the Bjørnøya Basin, seismic interpretation (Figures 4 and 9) shows flat-layered deposition pierced by a salt diapir with a few isolated faults. The seismic observations hint that basin extension and crustal stretching were mostly accommodated by a major detachment fault and possibly a decollement level in the Permian salt layer (Gernigon et al., 2014). We note that rapid deposition and burial of a fine-gained muds represent the ideal conditions for overpressure. This is corroborated by low seismic velocities in the deepest part of the basin from expanding spread profiles (Jackson et al., 1990). For all those reasons, we postulate that seawater is the primary fluid in the pore space in these overpressured marine shales.

### 5.2.2 Bulk resistivity vs. porosity for various fluid salinity

To investigate the electrical resistivity anomaly of the Aptian-Albian marine shales, we use the Hashin-Shtrikman upper bound ( $HS^+$ ) that provides an upper limit on the effective conductivity of a two-phase, isotropic medium (Hashin and Shtrikman, 1962). As opposed to the purely

empirical Archie's law,  $HS^+$  is a theoretical result:

$$\frac{1}{\rho_{bulk}} = \sigma_{bulk} = \sigma_e + \frac{1 - \Phi}{\frac{1}{\sigma_s - \sigma_e} + \frac{\Phi}{3\sigma_e}} \quad (7)$$

In Figure 10, we present the results of calculation of the analytical " $HS^+$ " bulk resistivity  $\rho_{bulk}$  (Equation (7)) - porosity  $\Phi$  relationship in the Early Aptian - Albian marine shales. We use a mineral matrix conductivity of  $\sigma_s = 10^4 \Omega.m$  and six different pore fluids  $\sigma_e$  with increasing salinity from 3.5 wt% (seawater) to 20 wt%. The numerical experiment is conducted for a rock formation at T-P conditions mimicking that of sediments buried at 8 to 10 km depth, assuming lithostatic pressure and a geothermal gradient of 30 K/km. The relationship between fluid conductivity  $\sigma_e$  and salinity is also dependent on T-P conditions; we use a least-squared empirical relationships whose coefficients are determined in Tables 2 and 3 of Sakuma and Ichiki (2016).

The  $HS^+$  model suggests that in order to produce a bulk anomaly  $\rho_{bulk} < 1 \Omega.m$  with seawater as sole pore fluid, the porosity of the Aptian-Albian marine shales would have to be beyond  $\Phi > 6 \%$  at a burial depth of 8 - 10 km (Athy, 1930). Porosity values of marine shales at 6 km depth are consistently below 1% regardless of its mineralogy and thermal gradient(Yang and Guo, 2020). Such empirical result is obtained by numerical experiments on marine shales mechanical compaction and thermal state. However, the contribution of overpressure to the preservation of porosity is not taken into account in the model and remain uncertain. Assuming a doubling of porosity with overpressure, a 2% porosity value of marine shales buried at 8-10 km is a realistic and conservative choice.

With a porosity value of  $\Phi = 2\%$  in the overpressured layer, we find that a fluid salinity of 10 wt% is required to produce a bulk resistivity  $\rho_{bulk} = 1 \Omega.m$ , about 3 times the salinity of seawater. Following  $HS^+$ , we find that the probability of finding  $\rho_{bulk} < 1 \Omega.m$  (Figure 9) is equivalent to the probability of finding hypersaline fluid in the Early Cretaceous marine shales. We conclude that there may be a secondary source of brine fluids in the Bjørnøya Basin and Veslemøy High to account for the conductive anomaly.

### 5.2.3 Clay mineral dehydration during burial

Clay dehydration refers to the process where water molecules bound to clay minerals are released during burial and diagenesis (Perry and Hower, 1972). Under increasing pressure and temperature, smectite-to-illite (S-I) transformation (Perry and Hower, 1972) releases silica and water, reducing porosity and inducing high pore-fluid pressure. The expulsion of mineral-bound

water by dehydration and S-I transformation may increase the pore fluid salinity with higher concentration of dissolved ions like sodium, magnesium and chloride. A purely diagenetic explanation for increased pore-fluid salinity and porosity preservation is certainly intriguing and cannot be ruled-out. However, this process is most commonly regarded as a minor contributor to overpressure in sedimentary basins (Osborne and Swarbrick, 1997; Wangen, 2001).

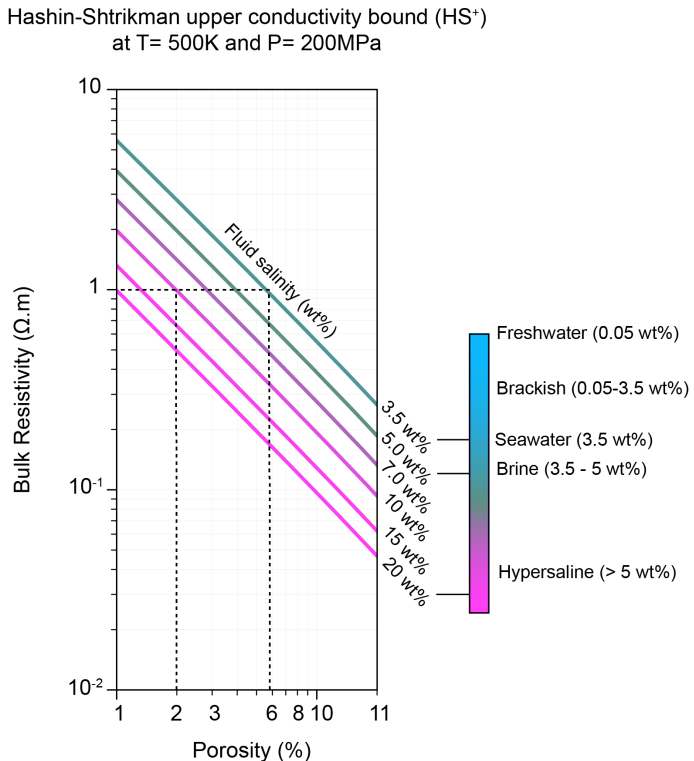


Figure 10: Bulk resistivity versus porosity for various fluid salinity at T-P conditions of the Aptian-Albian interval depth. The bulk resistivity model is based on the upper conductivity bound of the Hashin-Shtrikman model (Hashin and Shtrikman, 1962). The relationship between  $NaCl-H_2O$  fluid salinity and electrical conductivity at such burial depth is based on an empiric relationship scrutinized in Sakuma and Ichiki (2016).

### 5.3 Implications for fluid circulation in hyper-extended rift system

To find evidence of a secondary brine in the syn-tectonic sediments of hyper-extended rifts, one can look for rock outcrops, fluid inclusions in obducted or imbricated margins in orogenic systems. The circulations of deep saline or mantle-reacted fluids have been documented in two fossil systems: (1) saline fluids for Pyrenean rift basins, that recorded Early Cretaceous extension associated with mantle exhumation and high temperature metamorphism (Corre et al., 2018) and, (2) residual fluids from serpentization in the Alpine Tethys paleomargins (Pinto

et al., 2015).

In this section, we use those fossil rift systems to advocate for two different origin of secondary saline fluids in deep syn-tectonic sediments of the Bjørnøya Basin and Veslemøy High. Figure 11 summarizes the two alternative concepts for secondary brine circulation in hyper-extended basin.

We conclude that a hybrid model of saline fluid circulation, including both halite-derived brine and byproducts of serpentinization, are responsible for the high electrical conduction in the sediments.

### 5.3.1 The Pyrenean rift basins model: halite-derived brine fluids

In the Pyrenees, investigations of fluid inclusions advocate that brine fluids were squeezed out from Triassic halite layers and leached out to the syn-post rift Albian sediments during the hyper-extension phase (Corre et al., 2018; Nteme Mukonzo et al., 2021; Quesnel et al., 2019; Salardon et al., 2017). Pre-kinematic Triassic salt facilitated the extension by acting as decollement level and permitting fluid-salt interaction. The studies reveal fluid salinity ranging from 10 to 35 wt% (Nteme Mukonzo et al., 2021; Quesnel et al., 2019), compatible with salinity values explaining Aptian-Albian marine shales high conductivity in the SW Barents Sea using the  $HS^+$  model (Figure 10). In addition, seismic interpretation shows salt diapirs piercing through Early Cretaceous sediments in the Bjørnøya Basin (Figure 9). There is a potential analogy between the pre-kinematic Pyrenean Triassic halites and the Permian salt layer in the SW Barents Sea acting as decollement level during rifting.

As a results, the interaction of seawater (primary fluid), and halite-derived brine (secondary fluid) is a plausible explanation in the SW Barents Sea. In Figure 11a a sketch illustrates the circulation and mixing of salt-derived brine in syn-tectonic marine shales in a nascent hyper-extended basin.

### 5.3.2 The Alpine Tethys paleomargin model: residual fluids from serpentinization

In the paleomargins of Alpine Tethys, Pinto et al. (2015) argue that fluid circulation along detachment faults led to the modification of mineralogy and chemistry of mantle, crustal and sedimentary rocks. The authors found traces of mantle elements (Cr-Ni-V, Fe and Mn) in the

overlying crust and sediments. The latter study concludes that serpentinization occurred during the late phase of rifting when the residual crust was thinned enough to allow fluid circulation between the surface and the mantle. Normally, we expect the embrittlement of the crust when it reaches a thickness of 10 km, and the detachment fault is cross-cutting the continental crust. Detachment faults have played a major role in the Early Cretaceous rifting phase in the SW Barents Sea (Gernigon et al., 2014; Gresseth et al., 2021; Kairanov et al., 2021).

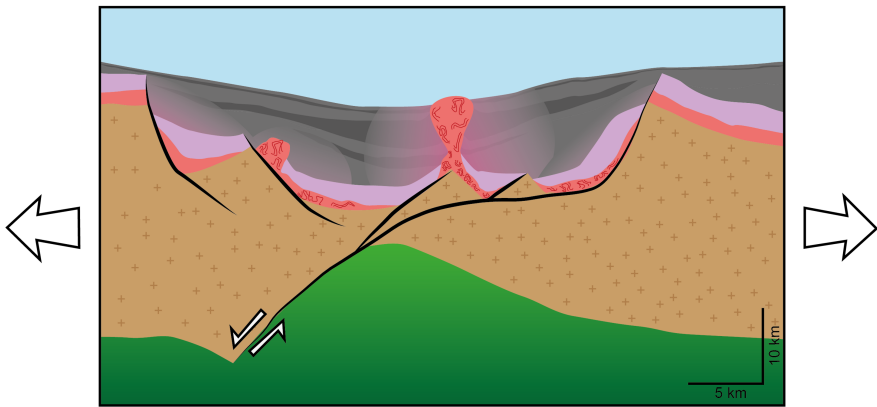
As a result, we propose another alternative model in Figure 11b where a secondary brine reservoir originates from residuals fluids from serpentinization, migrating along active detachments faults and contaminating the depositing seawater-filled marine shales.

## 6 Conclusion

We have successfully adapted the dimensionality compensation workflow (Seillé and Visser, 2020) to the SW Barents Sea and our target geological feature, by training a decision tree to recognize dimensionality effects in MT data and apply a corresponding compensation to observations in the Barents Sea. 1D Bayesian inversion of compensated MT data yielded an ensemble of 6000 1D resistivity models fitting the MT data was generated for 21 receivers located over the Bjørnøya Basin and Veslemøy High.

1. The statistical analysis of 1D posterior model distributions shows a very high probability of finding a bulk resistivity anomaly of  $\rho < 1 \Omega.m$  in the Early Aptian - Albian stratigraphic interval of the Bjørnøya Basin.
2. Following the  $HS^+$  model, the porosity of a seawater-filled marine shales would have to be superior to 6% to account for a bulk resistivity anomaly of  $\rho < 1 \Omega.m$ . Such porosity value is unreasonably high at a burial depth of 8 to 10 km.
3. Assuming a more realistic 2% porosity value, we find that the pore fluid needs to be at least 10 wt% (3 times more saline than seawater) to explain the high conductivity anomaly in the basin. A secondary source of brine fluids is thereby required.
4. Analysis of fluid inclusions and tracing of mantle elements in detachment faults of the Pyrenean rift basins and Alpine Tethys paleomargin reveals two possible origin for secondary brine reservoir in SW Barents Sea: halite-derived brine from Permian salt layer and residuals fluids from serpentinization (Figure 11).

a. "Pyrenean rift basins model": salt-derived brine fluid circulation



b. "Alpine Tethys paleomargin model": mantle-reacted fluid circulation

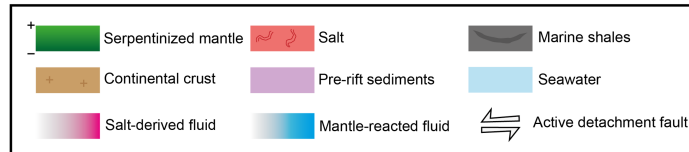
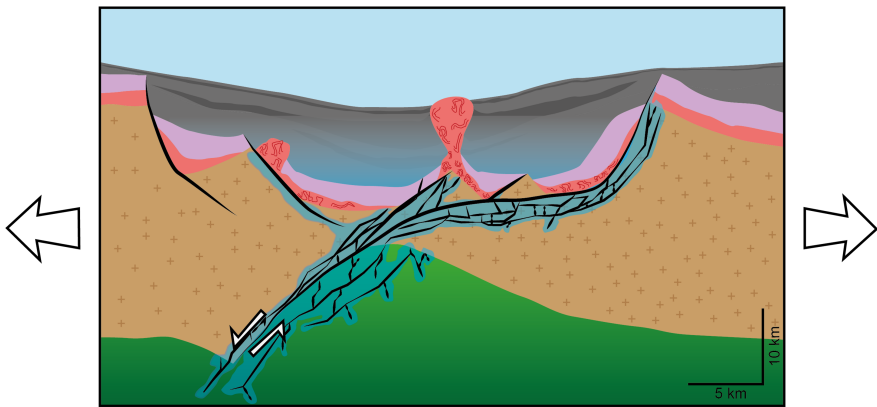


Figure 11: Generic models for secondary brine circulation during syn- to post-rift deposition of marine shales in a typical hyper-extended basin. a) "Pyrenean rift basins model": salt-derived brine fluids are squeezed out of the halite layer and leached out to the syn- to post-rift fine-grained marine muds. b) "Alpine Tethys paleomargin model": residual fluids from serpentinization of the upper mantle migrate along the damaged zone of the active detachment fault (fractures exaggerated on the illustration).

5. Both halite-derived and serpentinization residuals brine reservoirs are compatible with magnetotelluric, seismic and potential field data in the SW Barents.

## Acknowledgements

This work was funded by the Research Council of Norway through the industry PhD (project 298994) and SkatteFUNN (project 308897) schemes. JIF and SP also acknowledge support from the Research Council of Norway through its Centers of Excellence funding scheme, project number 223272 (CEED) and 228107 (ARCEEx). The authors would like to thank EMGS and TGS for allowing to use and publish MT and seismic reflection data, respectively, from their multiclient database. RC is particularly grateful to F. Roth, M. Hansen, P. Gåbrielsen, J.P. Morten, O.M. Pedersen and E. Bjørdal for enabling this project. Former EMGS colleagues are acknowledged for their implication in the development of EM technology and data acquisition in the Barents Sea. The authors would like to acknowledge G. Egbert, A. Kelbert and N. Meqbel for providing an academic license of ModEM. RC acknowledges comments from L. Gernigon about different models of brine fluids in hyper-extended basins that helped improve the discussion part.

## Data availability

The MT data underlying this article were provided by EMGS ASA under license / by permission. Data will be shared upon reasonable request to the corresponding author subject to permission of EMGS ASA.

## References

- Athy, L. F. (1930). Density, porosity, and compaction of sedimentary rocks. *AAPG Bulletin*, 14(1), 1–24. <https://doi.org/10.1306/3D93289E-16B1-11D7-8645000102C1865D>
- Bibby, H. M., Caldwell, T. G., & Brown, C. (2005). Determinable and non-determinable parameters of galvanic distortion in magnetotellurics. *Geophysical Journal International*, 163(3), 915–930. <https://doi.org/10.1111/j.1365-246X.2005.02779.x>
- Caldwell, T. G., Bibby, H. M., & Brown, C. (2004). The magnetotelluric phase tensor. *Geophysical Journal International*, 158(2), 457–469. <https://doi.org/10.1111/j.1365-246X.2004.02281.x>
- Corre, B., Boulvais, P., Boiron, M. C., Lagabrielle, Y., Marasi, L., & Clerc, C. (2018). Fluid circulations in response to mantle exhumation at the passive margin setting in the north pyrenean zone, france. *Mineralogy and Petrology*, 112(5), 647–670. <https://doi.org/10.1007/s00710-018-0559-x>
- Corseri, R., Planke, S., Faleide, J. I., Senger, K., Gelius, L. J., & Johansen, S. E. (2021). Opportunistic magnetotelluric transects from csem surveys in the barents sea. *Geophysical Journal International*. <https://doi.org/10.1093/gji/ggab312>
- Corseri, R., Planke, S., Gelius, L. J., Faleide, J. I., Senger, K., & Abdelmalak, M. M. (2023). Magnetotelluric image of a hyper-extended and serpentized rift system. *Earth and Planetary Science Letters*, 602. <https://doi.org/10.1016/j.epsl.2022.117914>
- Corseri, R., Faleide, T. S., Faleide, J. I., Midtkandal, I., Serck, C. S., Trulsvik, M., & Planke, S. (2018). A diverted submarine channel of early cretaceous age revealed by high-resolution seismic data, sw barents sea. *Marine and Petroleum Geology*, 98, 462–476. <https://doi.org/10.1016/j.marpetgeo.2018.08.037>
- Faleide, J. I., tsikalas, F., breivik, A. J., Mjelde, R., ritzmann, O., Engels, M., Wilson, P. G., & Eldholm, O. (2008). Structure and evolution of the continental margin off norway and the barents sea. *Episodes*.
- Gernigon, L., Brönner, M., Roberts, D., Olesen, O., Nasuti, A., & Yamasaki, T. (2014). Crustal and basin evolution of the southwestern barents sea: From caledonian orogeny to continental breakup. *Tectonics*, 33(4), 347–373. <https://doi.org/10.1002/2013tc003439>
- Gresseth, J. L. S., Braathen, A., Serck, C. S., Faleide, J. I., & Osmundsen, P. T. (2021). Late paleozoic supradetachment basin configuration in the southwestern barents sea -

- intrabasement seismic facies of the fingerdjupet subbasin. *Basin Research*. <https://doi.org/10.1111/bre.12631>
- Hashin, Z., & Shtrikman, S. (1962). A variational approach to the theory of the elastic behaviour of multiphase materials. *Journal of the Mechanics and Physics of Solids*, 11(2), 127–140. [https://doi.org/https://doi.org/10.1016/0022-5096\(63\)90060-7](https://doi.org/https://doi.org/10.1016/0022-5096(63)90060-7)
- Jackson, H. R., Faleide, J. I., & Eldholm, O. (1990). Crustal structure of the sheared south-western barents sea continental margin. *Marine Geology*.
- Jones, A. G. (2012). Distortion of magnetotelluric data: Its identification and removal. In *The magnetotelluric method* (pp. 219–302). <https://doi.org/10.1017/cbo9781139020138.008>
- Kairanov, B., Escalona, A., Norton, I., & Abrahamson, P. (2021). Early cretaceous evolution of the tromsø basin, sw barents sea, norway. *Marine and Petroleum Geology*, 123. <https://doi.org/10.1016/j.marpetgeo.2020.104714>
- Kelbert, A., Meqbel, N., Egbert, G. D., & Tandon, K. (2014). Modem: A modular system for inversion of electromagnetic geophysical data. *Computers and Geosciences*, 66, 40–53. <https://doi.org/10.1016/j.cageo.2014.01.010>
- Ledo, J. (2005). 2-d versus 3-d magnetotelluric data interpretation. *Surveys in Geophysics*, 26(5), 511–543. <https://doi.org/10.1007/s10712-005-1757-8>
- Lundin, E. R., & Doré, A. G. (2019). Non-wilsonian break-up predisposed by transforms: Examples from the north atlantic and arctic. *Geological Society, London, Special Publications*, 470(1), 375–392. <https://doi.org/10.1144/sp470.6>
- Midtkandal, I., Faleide, J. I., Faleide, T. S., Serck, C. S., Planke, S., Corseri, R., Dimitriou, M., & Nystuen, J. P. (2019). Lower cretaceous barents sea strata: Epicontinental basin configuration, timing, correlation and depositional dynamics. *Geological Magazine*, 1–19. <https://doi.org/10.1017/s0016756819000918>
- Nteme Mukonzo, J., Boiron, M.-C., Lagabrielle, Y., Cathelineau, M., & Quesnel, B. (2021). Fluid–rock interactions along detachment faults during continental rifting and mantle exhumation: The case of the urdach lherzolite body (north pyrenees). *Journal of the Geological Society*, 178(2). <https://doi.org/10.1144/jgs2020-116>
- Osborne, M. J., & Swarbrick, R. E. (1997). Mechanisms for generating overpressure in sedimentary basins: A reevaluation1. *AAPG Bulletin*, 81(6).
- Perry, E. T., & Hower. (1972). Late-stage dehydration in deeply buried pelitic sediments. *AAPG Bulletin*, 56, 2013–2021.
- Pinto, V. H. G., Manatschal, G., Karpooff, A. M., & Viana, A. (2015). Tracing mantle-reacted fluids in magma-poor rifted margins: The example of alpine tethyan rifted margins.

*Geochemistry, Geophysics, Geosystems*, 16(9), 3271–3308. <https://doi.org/10.1002/2015gc005830>

- Quesnel, B., Boiron, M.-C., Cathelineau, M., Truche, L., Rigaudier, T., Bardoux, G., Agrinier, P., de Saint Blanquat, M., Masini, E., & Gaucher, E. C. (2019). Nature and origin of mineralizing fluids in hyperextensional systems: The case of cretaceous mg metasomatism in the pyrenees. *Geofluids*, 2019, 1–18. <https://doi.org/10.1155/2019/7213050>
- Sakuma, H., & Ichiki, M. (2016). Electrical conductivity of nacl-h<sub>2</sub>o fluid in the crust. *Journal of Geophysical Research: Solid Earth*, 121(2), 577–594. <https://doi.org/10.1002/2015jb012219>
- Salardon, R., Carpentier, C., Bellahsen, N., Pironon, J., & France-Lanord, C. (2017). Interactions between tectonics and fluid circulations in an inverted hyper-extended basin: Example of mesozoic carbonate rocks of the western north pyrenean zone (chaînons béarnais, france). *Marine and Petroleum Geology*, 80, 563–586. <https://doi.org/10.1016/j.marpetgeo.2016.11.018>
- Seillé, H., & Visser, G. (2020). Bayesian inversion of magnetotelluric data considering dimensionality discrepancies. *Geophysical Journal International*, 223(3), 1565–1583. <https://doi.org/10.1093/gji/ggaa391>
- Seillé, H., Visser, G., Markov, J., & Simpson, J. (2021). Probabilistic cover-basement interface map in cloncurry, australia, using magnetotelluric soundings. *Journal of Geophysical Research: Solid Earth*, 126(7). <https://doi.org/10.1029/2021jb021883>
- Serck, C. S., Faleide, J. I., Braathen, A., Kjølhamar, B., & Escalona, A. (2017). Jurassic to early cretaceous basin configuration(s) in the fingerdjupet subbasin, sw barents sea. *Marine and Petroleum Geology*, 86, 874–891. <https://doi.org/10.1016/j.marpetgeo.2017.06.044>
- Tarantola, A. (2005). *Inverse problem theory and methods for model parameter estimation*. Society for Industrial; Applied Mathematics. <https://doi.org/https://doi.org/10.1137/1.9780898717921>
- Wangen, M. (2001). A quantitative comparison of some mechanisms generating overpressure in sedimentary basins. *tectonophysics*, 304, 211–234. [https://doi.org/https://doi.org/10.1016/S0040-1951\(01\)00064-6](https://doi.org/https://doi.org/10.1016/S0040-1951(01)00064-6)
- Yang, X.-G., & Guo, S.-B. (2020). Porosity model and pore evolution of transitional shales: An example from the southern north china basin. *Petroleum Science*, 17(6), 1512–1526. <https://doi.org/10.1007/s12182-020-00481-7>